Theory of magnetic phases of hexagonal rare earth manganites

Theory of magnetic phases of hexagonal rare earth manganites

I Munawar and S H Curnoe

Department of Physics and Physical Oceanography, Memorial University of Newfoundland,
St John's, Newfoundland & Labrador, A1B 3X7, Canada

E-mail: curnoe@physics.mun.ca

Abstract

The magnetic phases of hexagonal perovskites $RMnO_3$ (R = Ho, Er, Tm, Yb, Sc, Y) are analysed using group theory and the Landau theory of phase transitions. The competition between various magnetic order parameters is discussed in the context of antiferromagnetic interactions. A phenomenological model based on four one-dimensional magnetic order parameters is developed and studied numerically. It is shown that coupling of the various order parameters leads to a complex magnetic field–temperature phase diagram, and the results are compared to other experiments.

(Some figures in this article are in colour only in the electronic version)

1. Introduction

Hexagonal perovskites $RMnO_3$ (R = Ho, Er, Tm, Yb, Lu, Y or Sc) belong to an unusual class of materials known as 'multiferroics', which simultaneously display electric and magnetic ordering. Most of the hexagonal manganites are ferroelectric below a very high temperature ($T_c \approx 900$ K), and order magnetically at a lower temperature ($T_N \approx 100$ K). A complex phase diagram involving different magnetic order parameters (OPs) has been investigated using second harmonic generation [2, 3, 1], neutron scattering [4] and heat capacity measurements [5]. Perhaps the most intriguing and technologically promising development is the recent observation of the magnetoelectric effect in the low-temperature region of the phase diagram of $HoMnO_3$ [6, 7]. There are also indications of strong magneto-elastic coupling in $HoMnO_3$ [8].

The manganese and rare earth spins in $RMnO_3$ are nearly geometrically frustrated because of a slightly imperfect triangular lattice structure. Frustration is lifted by the onset of well-defined magnetic phases, each of which is associated either with a non-collinear spin structure within the hexagonal plane or antiferromagnetic ordering along the c-axis. The various
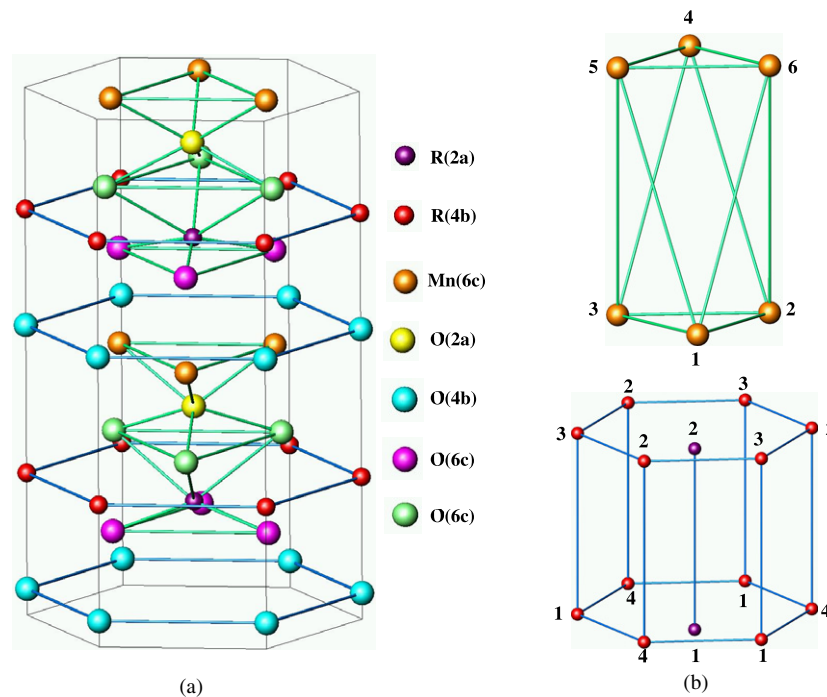
Figure 1. (a) Atomic positions in a single hexagonal primitive cell of $RMnO_3$. (b) Numbered Mn ions at the (6c) positions (top) and rare earth ions at the (4b) and (2a) positions (bottom).

magnetic phases have very similar antiferromagnetic (AF) interaction energies, due to the almost perfect triangular lattice, which results in a close competition between them.

In each $RMnO_3$, the magnetic phase B_2 appears in zero magnetic field at the temperature T_N, while the phase A_2 develops in magnetic fields of the order of a few tesla. These two phases are associated with ordering of Mn^{3+} spins within the hexagonal plane and are separated by a broad region of hysteresis. Additional phases appear at low temperatures in $HoMnO_3$ [9]. A sharp Mn spin-reorientation transition occurs at $T_{SR} \approx 33$ K, which results in the appearance of a third magnetic phase, B_1 [10]. Below 33 K, a new intermediate phase, which exhibits the magneto-electric effect, has been found in the region between the B_1 and B_2 phases [6, 11]. Moreover, a fourth magnetic phase, A_1, has been observed below 4 K due to ordering of Ho^{3+} spins [12].

In section 2 we describe the spin structures associated with each magnetic phase, and the antiferromagnetic competition between them. In section 3 we present a Landau model[1] which describes the four magnetic phases seen experimentally and numerical simulations of phase diagrams derived from the model. In section 4 we discuss our results.

2. Crystal and magnetic structure

Below T_c, hexagonal $RMnO_3$ has the space group symmetry $P6_3cm$ (#185, C_{6v}^3) [14]. The crystal structure of $RMnO_3$ is shown in figure 1(a). With six chemical formula units per unit cell, the Mn^{3+} ions occupy the (6c) positions, and form triangular lattices on the z and $z + 1/2$

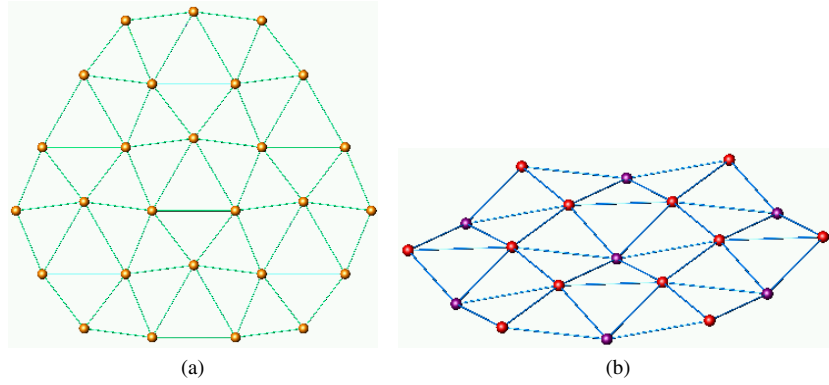[1] A preliminary version of this work appeared in [13].

Figure 2. Triangular lattices formed by (a) Mn ions (viewed parallel to the c-axis) and (b) rare earth ions (viewed at an angle with respect to the c-axis).

planes. The (6c) positions are $(x, 0, z)$ and equivalent, where $x \approx 1/3$ and $z = 0$. $x = 1/3$ yields a perfect triangular lattice. The rare earth ions occupy (2a) and (4b) positions, which are $(0, 0, z)$ (and equivalent, with $z = 0.22$) and $(1/3, 2/3, z)$ (and equivalent, with $z = 0.27$) respectively. A perfect triangular lattice is formed when the two z-parameters are equal. The triangular lattices formed by the Mn and rare earth ions are shown in figure 2.

The point group C_{6v} has four one-dimensional (1D) irreducible representations (IRs), A_1, A_2, B_1 and B_2, and two two-dimensional IRs E_1 and E_2. The same notation is used to label magnetic representations, where the characters -1 in the character table of C_{6v} indicate a combination of the point group element with time reversal[2]. For the 1D representations, the same names are given to the corresponding magnetic phases. In the presence of magnetic order parameters, the magnetic space groups are $P6_3cm$ (A_1), $P6_3\underline{cm}$ (A_2), $P\underline{6}_3cm$ (B_1), and $P\underline{6}_3\underline{cm}$ (B_2).

The spin configurations of rare earth and Mn ions may be classified according to the magnetic representations by which they transform. All configurations which transform according to 1D representations are listed in table 1, where the spin subscripts refer to the atom numbers shown in figure 1(b). The remaining degrees of freedom are accommodated by the 2D representations of C_{6v}; but so far, there is no evidence that phases corresponding to 2D OPs appear in the phase diagram, so the 2D spin configurations are not included here.

We now discuss general features of the H–T phase diagrams of RMnO$_3$ by considering the relative strength of the nearest-neighbour antiferromagnetic interaction for each spin configuration in table 1. The antiferromagnetic interaction is defined as

$$I = \tfrac{1}{2}J \sum_{\langle ij \rangle} \hat{S}_i \cdot \hat{S}_j \tag{1}$$

where the sum is over nearest neighbours and $\hat{S}_i$ is a spin operator. The parameter J depends on the distance between nearest neighbours.

The first four configurations for Mn ions listed in table 1, and illustrated in figure 3, confine the spins to the hexagonal plane. The B_2 phase that appears below T_c, the A_2 phase found in magnetic fields, and the B_1 phase found at lower temperature in HoMnO$_3$ are due to these configurations. In order to compare the AF interaction strengths for the different configurations, first, sets of nearest neighbours should be separated into three cases, according to symmetry. The first case is the set of coplanar nearest neighbours ({1, 2, 3} and {4, 5, 6}, numbered as in

---

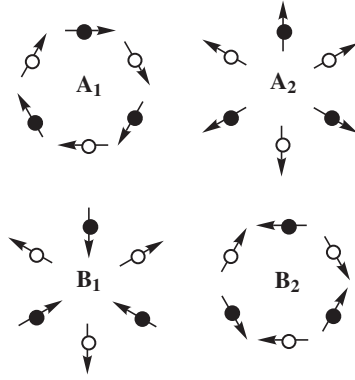[2] We use the notation found in [15].

Figure 3. Manganese spin configurations in the hexagonal plane. These correspond to the first four (6c) configurations listed in table 1 (after [1]).

Table 1. 1D spin configurations classified by irreducible representation. The rare earth spin configurations are shown in figure 4 and the first four Mn (6c) configurations are shown in figure 3.

R (2a)	A_2	$S_{1z} + S_{2z}$
	B_1	$S_{1z} - S_{2z}$
R (4b)	A_1	$S_{1z} + S_{2z} - S_{3z} - S_{4z}$
	A_2	$S_{1z} + S_{2z} + S_{3z} + S_{4z}$
	B_1	$S_{1z} - S_{2z} - S_{3z} + S_{4z}$
	B_2	$S_{1z} - S_{2z} + S_{3z} - S_{4z}$
Mn (6c)	A_1	$-(S_{1x} - S_{4x}) + \frac{1}{2}(S_{2x} + S_{3x} - S_{5x} - S_{6x})$ $+ \frac{\sqrt{3}}{2}(-S_{2y} + S_{3y} + S_{5y} - S_{6y})$
	A_2	$-(S_{1y} - S_{4y}) + \frac{\sqrt{3}}{2}(S_{2x} - S_{3x} - S_{5x} + S_{6x})$ $+ \frac{1}{2}(S_{2y} + S_{3y} - S_{5y} - S_{6y})$
	B_1	$-(S_{1y} + S_{4y}) + \frac{\sqrt{3}}{2}(S_{2x} - S_{3x} + S_{5x} - S_{6x})$ $+ \frac{1}{2}(S_{2y} + S_{3y} + S_{5y} + S_{6y})$
	B_2	$-(S_{1x} + S_{4x}) + \frac{1}{2}(S_{2x} + S_{3x} + S_{5x} + S_{6x})$ $+ \frac{\sqrt{3}}{2}(-S_{2y} + S_{3y} - S_{5y} + S_{6y})$
	A_2	$S_{1z} + S_{2z} + S_{3z} + S_{4z} + S_{5z} + S_{6z}$
	B_1	$S_{1z} + S_{2z} + S_{3z} - S_{4z} - S_{5z} - S_{6z}$

figure 1(b)). In this case, the AF interaction is the same for all four configurations, $I = -Js^2$. The second and third cases involve non-coplanar pairs. The second case pairs ions on opposite sides of the hexagonal primitive cell ($\{1, 4\}, \{2, 5\}, \{3, 6\}$) and the third case is the remaining pairs. The second case favours A_1 and A_2 equally, while the third case favours B_1 and B_2 equally, with $I = \pm Js^2$ in both cases. The distance between partners in each pair for the second and third cases is exactly the same if the Mn position parameter x is exactly $1/3$. Deviations away from $x = 1/3$ will favour either the A phases or the B phases. However, the observed behaviour is the opposite of what could be expected. At higher temperatures (75 K) $x = 0.338(1)$ [4], which brings the second case pairs closer together and favours the A phases, but the B_2 phase is observed. At the lowest temperature (1.5 K) $x = 0.330(1)$ the B phases are favoured but the A_1 phase is observed. The subtle competition between all four phases which results in the dominance of the B_2 phase at high temperatures is most likely to be resolved by the inclusion of other interactions, such as next-nearest-neighbour, or interactions with the rare earth ions.
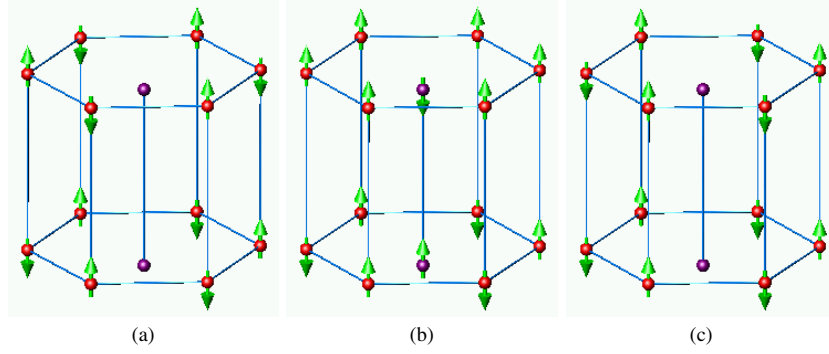
Figure 4. Rare earth spin configurations for (a) A_1, (b) B_1 and (c) B_2 configurations for (2a) and (4b) positions listed in table 1.

In HoMnO$_3$, additional phases B_1 followed by A_1 appear as the temperature is further lowered. The B_1 phase is associated both with in-plane Mn moments and Ho ordering along the c-axis. The (2a) and (4b) holmium ions are almost coplanar. The B_1 phase is AF along the c-axis for (2a) and (4b) ions, but inside the hexagonal plane the (4b) ions are aligned ferromagnetically with each other, and antiferromagnetically with the (2a) ions. This is shown in figure 4(b).

At the lowest temperatures, the A_1 configuration emerges, which has AF ordering of the (4b) spins in the planes and along the c-axis, as shown in figure 4(a). Then, there can be no AF arrangement with respect to the (2a) positions (because there is no A_1 configuration for them). The phase transition from B_1 to A_1 is first-order, as is the case between all transitions involving different order parameters; therefore hysteresis is anticipated, both on phenomenological grounds, and also because of the persistence of the B_1 configuration on the (2a) positions.

The total in-plane AF interaction energy for all Ho ions is approximately the same for all three configurations shown in figure 4. In all cases $I = -2Js^2$, but J differs according to the distance between ions. If the (2a) and (4b) position parameters z are equal then the three phases are degenerate; otherwise A_1 and B_2 have lower energy. The collinear AF interactions favour the B_1 configuration, with $I = -3Js^2$ (versus $I = -2Js^2$ for A_1 and $I = 2Js^2$ for B_2).

The A_2 phase will always dominate at high enough magnetic fields, since it transforms in the same way as the applied field, and couples linearly in the phenomenological sense. Microscopically, Zeeman coupling to Mn or Ho spins induces ferromagnetic order associated with the A_2 phase.

3. Landau model and phase diagram

The order parameters of the phases A_1, A_2, B_1 and B_2 are denoted by η_1, η_2, η_3 and η_4, respectively. The minimal Landau model which describes the A_2 and B_2 phases, observed in all RMnO$_3$, is

$$F = \alpha_2\eta_2^2 + \beta_2\eta_2^4 + \alpha_4\eta_4^2 + \beta_4\eta_4^4 + \gamma_{24}\eta_2^2\eta_4^2 - H_z(\rho_1\eta_2 + \rho_2\eta_2^3 + \rho_3\eta_2\eta_4^2) \qquad (2)$$

where α_i, β_i and γ_{ij} and ρ_i are phenomenological coupling constants and H_z is the magnetic field parallel to the c-axis. The coefficients α_i are temperature dependent, $\alpha_i = a_i(T - T_i)$, where T_i is the temperature limit of stability for each phase (which for convenience, we call the 'transition temperature'), and $\beta_i > 0$ is required for stability. α_4 changes sign at $T_N \approx 100$ K in all RMnO$_3$.

In zero applied field, the model allows for four different phases: $(0, 0)$ (the parent phase), which may be connected to either $(\eta_2, 0)$ (A_2-phase), $(0, \eta_4)$ (B_2-phase) or (η_2, η_4) (mixed phase) by second-order phase transitions. These are found by solving the set of coupled equations $\partial F/\partial \eta_i = 0$, subject to the minimization conditions $(\partial^2 F/\partial \eta_2^2) > 0$ and $(\partial^2 F/\partial \eta_2^2)(\partial^2 F/\partial \eta_4^2) - (\partial^2 F/\partial \eta_2 \partial \eta_4)^2 > 0$. The model also allows for the coexistence of two or more different phases by hysteresis.

The mixed phase (η_2, η_4) can be a minimum of F only when $4\beta_2\beta_4 > \gamma_{24}^2$. Its existence is *not* the result of hysteresis. Anomalies in the c-axis magnetization at the B_2 phase boundary [5] are evidence that B_2 and A_2 are coupled (i.e. $\gamma_{24} \neq 0$). In general, η_2 grows linearly with applied field but it may still be subject to a transition in the sense that a change in sign of α_2 will increase the number of minima of the Landau functional.

Additional order parameters η_1 and η_3 are required to describe the additional phases observed in HoMnO$_3$. Additional terms in the free energy include those obtained by replacing in (2) η_4^2 by η_1^2 and η_3^2, as well as terms of the form $\eta_1\eta_2\eta_3\eta_4$ and $H_z\eta_1\eta_3\eta_4$.

The Landau model describing A_1, A_2, B_1 and B_2 phases is

$$
\begin{aligned}
F(\eta_1, \eta_2, \eta_3, \eta_4) = {} & F(\eta_2, \eta_4) + \alpha_1\eta_1^2 + \beta_1\eta_1^4 + \alpha_3\eta_3^2 + \beta_3\eta_3^4 + \gamma_{12}\eta_1^2\eta_2^2 \\
& + \gamma_{13}\eta_1^2\eta_3^2 + \gamma_{14}\eta_1^2\eta_4^2 + \gamma_{23}\eta_2^2\eta_3^2 + \gamma_{34}\eta_3^2\eta_4^2 + \gamma\eta_1\eta_2\eta_3\eta_4 \\
& - H_z(\rho_4\eta_2\eta_3^2 + \rho_5\eta_2\eta_1^2 + \rho_6\eta_1\eta_3\eta_4).
\end{aligned}
\tag{3}
$$

This model may be solved exactly in zero applied field, and it is found that the allowed phases are $(0, 0, 0, 0)$ (the parent phase), $(\eta_1, 0, 0, 0)$ etc (A_i or B_i) and $(\eta_1, \eta_2, 0, 0)$ etc (mixed phases involving two order parameters). In addition, two or more phases may coexist due to hysteresis.

The models (2) and (3) were analysed by varying the temperature and field and searching for the minima of F numerically. Typically, several minima were present, the deepest corresponding to the true ground state and the rest to metastable states observed as hysteresis. Each set of parameters α, β, γ and ρ yields a different phase diagram; these parameters were varied to find the best match to phase diagrams obtained in experiments [1, 5, 12, 16].

Figure 5 shows numerical simulations of the phase diagrams for RMnO$_3$, modelled by (2). In all four diagrams, the onset of the B_2 phase for $H = 0$ is determined by setting $T_4 = 80$ K. Below this temperature two minima corresponding to non-zero η_4 occur in (2). The A_2 phase, which dominates the right-hand side (high field region) of all diagrams, corresponds to a Landau functional which has only *one* minimum that is shifted away from $\eta_2 = 0$ because of the term $H_z\eta_2$. Thus the free energy resembles the parent phase but the symmetry is A_2. In figures 5(b), (c) and (d) hysteresis occurs, indicated by lighter coloured areas near the black phase boundary line. Here the free energy has three minima, one corresponding to the field-shifted parent phase, and two to the B_2 phase. In figures 5(a), (b) and (d) we have $\gamma_{24}^2 < 4\beta_2\beta_4$, so a pair of minima for $\eta_2 \neq 0$ never occurs. However, in figure 5(c), $\gamma_{24}^2 > 4\beta_2\beta_4$, so two shallow minima for η_2 coexist with two for η_4 in the bottom left-hand corner of the phase diagram. Figure 5(b) shows the correct arrangement of phases on the phase diagram compared to experiments, but fails to simulate correctly the curvature of the phase boundary. Figure 5(d), which includes the nonlinear (in OP) field-dependent terms in (2), is a significant improvement.

Figure 6 shows numerical simulations of the phase diagram of HoMnO$_3$, modelled by (3). The upper part of the diagrams, showing the B_2 and A_2 phases, is similar to RMnO$_3$, in that the B_2 phase appears below the transition temperature $T_4 = 75$ K, and the A_2 phase is induced by the magnetic field. Non-zero transition temperatures T_i were assigned to all other phases ($T_1 = 52$ K, $T_2 = 39$ K, $T_3 = 62$ K) below which the phases are metastable and hysteresis occurs. True phase transitions occur below the transition temperatures, along the lines where the free energies, evaluated for different phases, are equal. Different shades within a single phase represent the presence of other, metastable phases. Figure 6(a) bears a poor resemblance
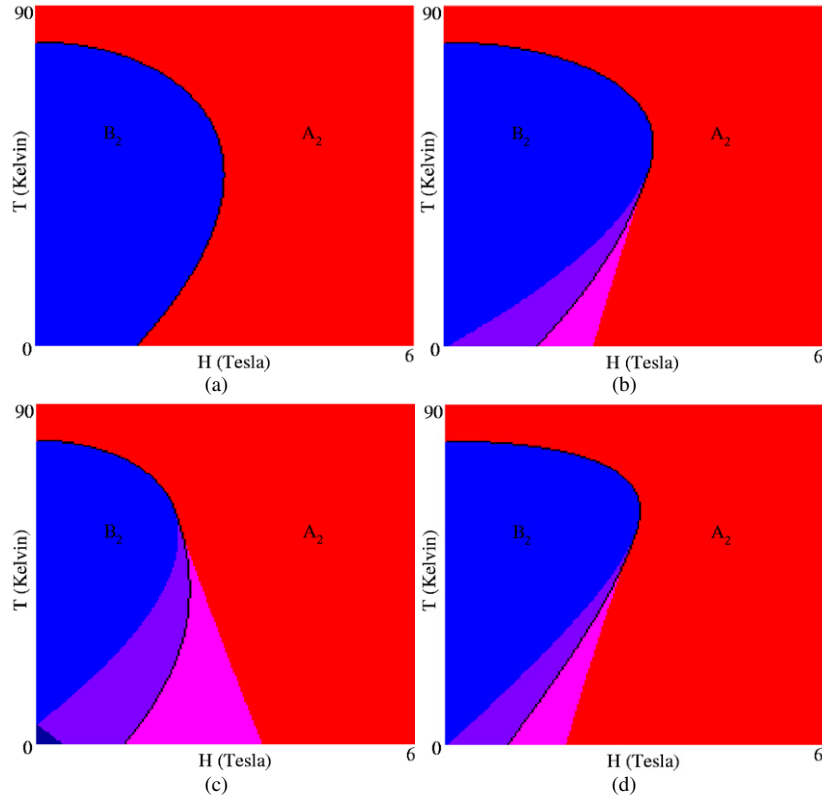
Figure 5. Numerical simulations of the phase diagram of $RMnO_3$. The black line is the boundary between the A_2 and B_2 phases. Hysteresis occurs in the lighter-coloured regions. In all four diagrams $T_4 = 80$ K, $T_2 = 10$ K, $\beta_2 = 10$, $\beta_4 = 100$ and $\rho_1 = 12$, while $\gamma_{24} = 60$, 150, 300 and 150 in (a), (b), (c) and (d), respectively. The parameters a_i ($\alpha_i = a_i(T - T_i)$) were scaled to unity. Nonlinear field-dependent coefficients $\rho_2 = \rho_3 = 5$ are introduced in diagram (d).

to experiments. Figure 6(b), which includes nonlinear field-dependent terms, is significantly better, but still fails to reproduce qualitatively all of the phase boundary around the B_1 phase as seen in experiments.

4. Discussion

In section 2 we argued that, even in the absence of true geometrical frustration, there is not enough information to predict the magnetic ground state without detailed knowledge of the AF interaction strength J. In Landau theory, the microscopic model (1) is replaced by a phenomenological one (2), (3), and the parameter J is incorporated into the temperature-dependent α_i. Landau theory includes all interactions allowed by symmetry, and as such is more general than the AF interaction, which is isotropic. However, the proliferation of phenomenological constants also inhibits the predictive powers of the Landau model. Nevertheless, Landau modelling is useful because it can reveal the minimal elements in a theory that are needed to describe the phase diagrams of $RMnO_3$. In our analysis, we found that a model based on the usual second- and fourth-order terms, and a linear coupling of the order parameter to the magnetic field, does not describe well the observed phase diagrams, especially
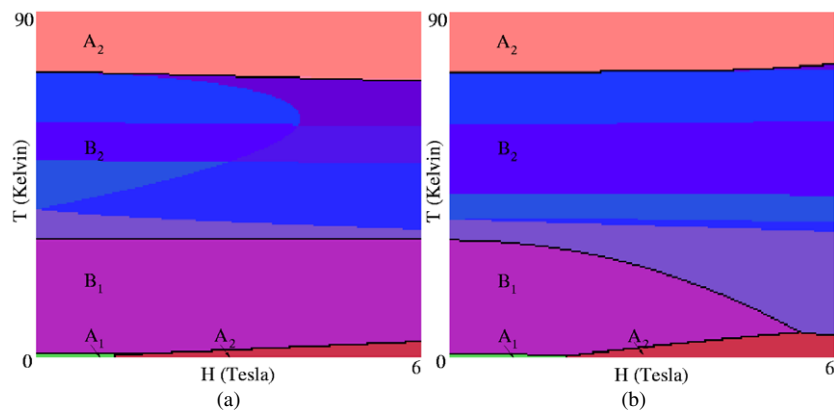
Figure 6. Numerical simulations of the phase diagram of $HoMnO_3$. Black lines separate the phases, while different shades within a phase represent the presence of other metastable states. In both diagrams $\beta_1 = 0.14$, $\beta_2 = 0.08$, $\beta_3 = 0.2$, $\beta_4 = 0.4$, while $\gamma_{12} = 1$, $\gamma_{13} = 1$, $\gamma_{14} = 1$, $\gamma_{23} = 6$, $\gamma_{24} = 2.9$, $\gamma_{34} = 10$, $\rho_1 = 1$ in (a) and $\gamma_{12} = 90$, $\gamma_{13} = \gamma_{14} = \gamma_{23} = \gamma_{24} = \gamma_{34} = 100$, $\rho_1 = 4$ in (b). Diagram (b) also includes nonlinear field-dependent terms $\rho_2 = 1$, $\rho_3 = 2$, $\rho_4 = 0.05$.

the curvature of the phase boundaries. The inclusion of nonlinear (in OP) field-dependent terms is a significant improvement.

The magneto-electric effect is observed in the region between the B_1 and B_2 phases. Linear coupling of the magnetic and electric fields of the form $\alpha_{ij} E_i B_j$ can only occur when both inversion and time reversal symmetry are absent—these are necessary but not sufficient conditions. A mixture of B_1 and B_2 order parameters (due to hysteresis) does not lower the symmetry enough for magnetoelectric coupling. However, domain walls, which connect different domains of the same phase, have been implicated in the observation of the magnetoelectric effect [6]. Thus OP gradient terms, which couple to the magnetic field, may significantly alter the free energy landscape, and could possibly replace the nonlinear field-dependent terms which we introduced.

In conclusion, we have studied phase diagrams for $RMnO_3$, using group theory and Landau theory, by including up to fourth-order phenomenological couplings between order parameters and nonlinear coupling to an applied magnetic field. Antiferromagnetic competition between magnetic phases, due to a near perfect triangular lattice structure, gives rise to a complex phase diagram. Our simulations reproduce the main features seen in experimental results, including the general arrangement of phases on the diagram, hysteresis effects and the curvature of phase boundaries.

Acknowledgments

References

[1] Fiebig M and Lottermoser Th 2003 *J. Appl. Phys.* **93** 8194
[2] Fröhlich D, Leute St, Pavlov V V, Pisarev R V and Kohn K 1999 *J. Appl. Phys.* **85** 4762
[3] Fiebig M, Fröhlich D, Kohn K, Lottermoser Th, Pavlov V V and Pisarev R V 2000 *Phys. Rev. Lett.* **84** 5620
[4] Lonkai Th, Hohlwein D, Ihringer J and Prandl W 2002 *Appl. Phys.* A **74** S843

[5] Lorenz B, Yen F, Gospodinov M M and Chu C W 2005 *Phys. Rev.* B **71** 014438
[6] Lottermoser Th and Fiebig M 2004 *Phys. Rev.* B **70** 220407
[7] Fiebig M 2005 *J. Phys. D: Appl. Phys.* **38** R123
[8] dela Cruz C, Yen F, Lorenz B, Wang Y Q, Sun Y Y, Gospodinov M M and Chu C W 2005 *Phys. Rev.* B **71** 060407
[9] Fiebig M, Degenhardt C and Pisarev R V 2002 *J. Appl. Phys.* **91** 8867
[10] Lorenz B, Litvinchuk A P, Gospodinov M M and Chu C W 2004 *Phys. Rev. Lett.* **92** 87204
[11] Lottermoser T, Lonkai T, Amann U, Hohlwein D, Ihringer J and Fiebig M 2004 *Nature* **430** 541
[12] Vajik O P, Kenzelmann M, Lynn J W, Kim S B and Cheong S W 2005 *Phys. Rev. Lett.* **94** 087601
[13] Curnoe S H and Munawar I 2006 *Proc. SCES '05*; *Physica* B **378–380** 554
[14] Yakel H L, Koehler W C, Bertaut E F and Forrat E F 1963 *Acta Crystallogr.* **16** 957
[15] Tinkham M 1964 *Group Theory and Quantum Mechanics* (New York: McGraw-Hill)
Tinkham M 2002 *International Tables for Crystallography* (Dordrecht: Kluwer)
[16] Yen F *et al* 2005 *Phys. Rev.* B **71** 180407